E JOURNAL

# Optimization of Additive Manufacturing Parameters for CoCrMo Alloy Using PBF-LB/M Manufacturing

## Effects on Density, Porosity, and Mechanical Properties

Tobias Trauner [a], Kevin Lippmann [a] , Maximilian Heinz [a], Fabian Riß [a]

[a] Technical University of Applied Sciences Rosenheim, Hochschulstr. 1, 83024 Rosenheim, Deutschland

**Abstract** Laser powder bed fusion of Cobalt-Chromium-Molybdenum for biomedical applications is well established and requires parameter windows that reliably meet ASTM F75 while remaining transferable across builds. Yet, machine specific process windows and the confirmatory validation are often under-reported. A two-level factorial design with 24 runs on a TruPrint1000 quantified the effects of laser power (115-175 W), scan speed (400-1300 mm/s), and hatch spacing (50-200 µm) on relative density, hardness, and tensile properties. The model was validated via replicate runs and a Monte Carlo robustness analysis (10,000 iterations at 1% failure probability). Hatch spacing dominated densification and mechanical response. The optimized and validated parameter set (laser power of 165.5 W, scan speed of 714 mm/s, hatch spacing of 63 µm, laser spot size of 55 µm, and layer thickness of 20 µm) corresponds to a volumetric energy density of 187 J/mm$^3$. This configuration achieved ρ higher than 99.75% and mechanical properties exceeding ASTM F75 requirements for tensile and yield strength, elongation, and hardness. These results confirm the suitability of the established parameters for producing high-performance Cobalt-Chromium-Molybdenum components. Future work may expand the validation to complex, implant-like geometries and include advanced three-dimensional pore characterization and support structure analyses to further link process robustness and functional implant performance.

## Introduction

Driven by the demand for better personalization of patient care, metal Additive Manufacturing (AM) has gained importance in the recent years. Among the available methods, Laser Powder Bed Fusion (PBF-LB/M) has emerged as a key technology due to its ability to fabricate geometrically complex structures with high precision and reproducibility [1, 2]. The Cobalt–Chromium–Molybdenum alloy Co28Cr6Mo is well established as a standard material for biomedical applications, owing to its excellent biocompatibility, corrosion resistance, and mechanical performance [3, 4]. To ensure clinical safety and functionality, fabricated components must comply with the requirements of ASTM F75, which defines the minimum mechanical property standards for surgical implant alloys [5, 6].

Although extensive research has been devoted to optimizing PBF-LB/M parameters, findings across studies remain divergent [7, 8]. Differences in machine architectures, process strategies, and alloy compositions have limited the transferability of published parameter sets to specific system–material combinations. Moreover, many investigations have primarily addressed the interaction of laser power (LP) and scan speed (SS). In contrast, other critical parameters such as hatch spacing (HS), layer thickness (LT), and laser spot size (LSS) have received comparatively little attention [6-9]. In particular, the role of HS in relation to mechanical properties and parameter interactions has not yet been fully clarified. As a dominant factor governing melt-pool overlap and the extent of remelting between adjacent scan tracks, HS may directly affect the continuity of the melt path, local heat accumulation, and ultimately the consolidation quality. An insufficient overlap may lead to lack-of-fusion porosity, whereas excessive overlap can promote overheating and surface instability [10, 11]. Understanding this balance is therefore essential for achieving both high density and consistent mechanical performance.

This lack of comprehensive, system-specific insights has hampered reliable prediction of process–structure–property relationships and the establishment of standardized guidelines for medical-grade Co28Cr6Mo processing.

The present study aims to systematically investigate the influence of LP, SS, and HS on the structural integrity and mechanical properties of AM Co28Cr6Mo. A structured Design of Experiments (DoE) approach was applied to identify parameter interactions and develop a predictive model linking process variables to mechanical performance indicators, including ultimate tensile strength (UTS), yield strength, elongation, hardness, density, and porosity. The overall objective is to define an optimized parameter set that consistently achieves part densities above 99.75% while fulfilling ASTM F75 requirements.

By generating new knowledge on parameter interactions in PBF-LB/M processing of Co28Cr6Mo, this study contributes to improving process reliability and material performance for biomedical applications. It should be noted that density and mechanical data were obtained from samples built with different powder states (respectively 100% fresh and 50/50% fresh–recycled), which may limit direct comparability. These findings provide a foundation for future optimization studies and are particularly relevant for the fabrication of complex, patient-specific geometries, including applications in shoulder implant design.

# Material and Methods

## Material and Machine

Co28Cr6Mo powder (Table 1) was processed using PBF-LB/M. Samples were manufactured on the TruPrint 1000 system (TRUMPF SE & Co. KG, Ditzingen, Germany) operating with a maximum LP of 200 W.

Table 1: Weight percentages of MetcoAdd F-75a Co28Cr6Mo and ASTM F75 requirements [12, 13].

| Name | Co [%] | Cr [%] | Mo [%] | C [%] | Other [%] |
|---|---|---|---|---|---|
| ASTM F75 | Balance | >27 | >5 | <0.35 | n.d. |
| MetcoAdd 75A | Balance | 28 | 6 | <0.2 | <1.0 |

## Experimental Design

A two-level full factorial DoE was applied to evaluate the influence of processing parameters on material properties. LP (115-175 W), SS (400-1300 mm/s), and HS (0.05 - 0.25 mm) were varied, while LT and LSS were kept constant. This configuration resulted in eight factorial design points, complemented by four center points to estimate curvature effects and assess reproducibility. An additional replicate run was performed to increase statistical power. In total, 24 samples were fabricated for screening, which yielded a statistical power of 96% (two-sided F-test, $\alpha = 0.05$), exceeding the recommended threshold of 80% for detecting significant effects [14]. Response variables were selected based on clinical relevance and material standards: relative density, porosity, Vickers hardness (HV5), UTS, yield strength, and elongation. Target values were defined according to ASTM F75 requirements (UTS higher than 655 MPa, yield strength higher than 450 MPa, elongation higher than 8%, hardness 250–320 HV, density higher than 99%). The factorial model included all main effects and two-factor interactions. Model quality was evaluated using standard fit statistics ($R^2$, $Q^2$, model validity, reproducibility). To avoid bias, the experimental run order was fully randomized. Depending on the model outcome, two pathways were predefined for model validation: Direct validation of the optimized parameter set, if model performance met quality thresholds ($R^2$ higher than 0.5, $Q^2$ higher than 0.5 [14]). Further optimization using response surface methodology (RSM), if additional refinement was required. This design allowed efficient identification of dominant factors and interactions while minimizing resource demand, ensuring reproducibility, and providing a statistically robust foundation for process optimization. The detailed DoE configuration and factor definitions are summarized in Tables A1-A3, and the corresponding experimental data are provided in Online Resource 1.

## Sample Fabrication

Two types of specimens were produced:

- Cubic samples (10 x 10 x 10 mm): used for porosity, density, and hardness analysis, manufactured from fresh powder. Preparation included embedding into green bakelite granulate, grinding, and polishing.
- Tensile samples (DIN 50125, Specimen A, $d_0 = 5$ mm): used for mechanical testing, produced from a 50/50 mixture of fresh and recycled powder, manufactured

vertically with respect to the build base. No mechanical preparation performed, tested in as-built condition.

The scan strategy was set to be bi-directional for both sample types. To prevent feedstock aging from acting as a hidden covariate that could distort densification trends, the separation of powder states was intentional. Cubes were designed to isolate parameter–densification effects under controlled feedstock conditions (fresh powder), whereas tensile specimens were built to assess mechanical performance under realistic recycling conditions (50/50 fresh–recycled blend). This approach enhances internal validity in the densification analysis and external validity in the mechanical evaluation, but it makes establishing a direct correlation between density and mechanical properties challenging. Accordingly, results are interpreted in the context of their respective experimental objectives. Samples were attached with support structures and mechanically separated from the build platform. No additional heat treatment was applied before testing. An overview linking the process parameters to the sample name is provided in Table A4.

## Material Characterization

Porosity was evaluated based on 2D cross-sectional (3 mm depth) image analysis using a custom MATLAB script developed in-house. Images were acquired with a Zeiss Axio Imager.M2.m microscope (Carl Zeiss Microscopy Deutschland GmbH, Oberkochen, Germany) using the automated Extended Depth of Focus function. The resulting composite image consisted of 12 connected subfields (3 × 4), covering almost the entire polished surface. Image resolution (µm/pixel) was either entered directly or interactively derived from the scale bar and used for all metric conversions. A Region of Interest was manually defined to exclude edges and mounting resin, typically representing ~90% of the visible cross-section. Prior to segmentation, the RGB images were converted to 8-bit greyscale. Depending on surface condition, Gaussian, median, anisotropic, or anisotropic diffusion filters were applied to reduce noise and remove minor scratches (Table A5), followed by adaptive binarization. Subsequently, watershed segmentation separated background and pore regions, enabling pore detection and quantification according to ASTM F1854 into micro- (<10 µm radius), meso- (10–100 µm), and macro-pores (>100 µm). A representative image processing workflow is provided in Figure A1 for reference. Supplementary cross-sectional images of representative specimens are available in Online Resource 2. Hardness testing was performed according to DIN SPEC 4864 using the HV5 method using the i3D-mBV system (Imprintec GmbH, Bochum, Germany). Each specimen was indented five times with a load of 49.03 N and a dwell time of 15 s. The diagonals of the indentation marks were measured, and the mean hardness value was calculated. Tensile testing followed DIN EN ISO 6892-1 at room temperature. Cylindrical specimens (Ø 5 mm, gauge length 30 mm) were tested using a 100 kN universal testing machine (ZwickRoell, Ulm, Germany) equipped with a MultiXtens extensometer (gauge length 20 mm). Samples were clamped axially and preloaded to 100 N before testing. The tests were performed at a constant crosshead speed of 10 mm/min until fracture. Force and displacement data were recorded at 20 ms intervals, and the resulting stress–strain curves were used to determine UTS, yield strength, and elongation. An overview of all tested specimens after destructive testing is provided in Figure A2, illustrating the fracture appearance within the test group. All characterization methods were aligned with ASTM F75 standard to ensure comparability with established requirements for medical-grade Co28Cr6Mo.

## Data Analysis

Statistical evaluation was conducted in MODDE 13.1 (Sartorius AG). The dataset was screened for outliers, and residual plots were examined to confirm the model assumptions. Analysis of variance (ANOVA) was applied to determine significant main effects and interactions. Model quality was evaluated by $R^2$ and $Q^2$ from cross-validation, with replicate runs included to assess reproducibility. To visualize parameter–response relationships, regression coefficients were plotted with 95% confidence intervals. Contour and design-space plots were then generated to identify parameter regions fulfilling ASTM F75 requirements. A Monte Carlo simulation was carried out to test the robustness of the HSxSS design space at LP = 165.5 W. The acceptance threshold was set to 1% failure probability, resolution to 64 and 10,000 iterations, and normally distributed random noise was added to the factors for the simulation (± 5% of the range of each factor). The number of simulated points $n_p$ and total of calculations $n_c$ are based on the number of responses $n_y$), resolution (r), number of factors ($n_f$), and iterations (I) as shown in Equation 1 and 2 [14].

$$n_p = n_y \cdot r^{n_f} \quad (1)$$

$$n_c = n_y \cdot r^{n_f} \cdot I \quad (2)$$

A total of 1310720 points were simulated to evaluate the most robust setpoint. The resulting most robust parameter set was subsequently confirmed by independent validation samples.

# Results

All builds were completed without interruptions or visible process failures. In total, 24 specimens per geometry were produced according to the DoE plan. A comparison between ASTM benchmarks and literature benchmarks is provided in Table 2.

Table 2: Summary of measured mechanical properties of 24 PBF-LB/M-processed Co28Cr6Mo samples compared to ASTM F75 requirements.

| Property | Unit | ASTM F75 | Value Range | Mean ± SD | Median | IQR |
|---|---|---|---|---|---|---|
| UTS | MPa | 655 | 207.73-1140.17 | 906.71±283.29 | 1018.25 | 105.17 |
| Yield Strength | MPa | 450 | 184.24-746.97 | 602.46±164.71 | 664.14 | 71.14 |
| Elongation | % | 8 | 0.38-22.99 | 11.91±6.39 | 12.86 | 6.87 |
| Hardness | HV | 250 | 76.95-406.50 | 336.51±104.63 | 381.70 | 33.65 |
| Porosity[2] | % | <1 | 0.02-46.92 | 7.36±13.89 | 1.33 | 3.24 |

[1] Minimum values according to ASTM F75

[2] Based on literature values reported by [6, 15]

Model validation and parameter relevance are illustrated in the residuals normal probability plots and regression coefficient diagrams (Appendix Figures A3-A8), confirming residual normality and highlighting the dominant effects and interactions within the models. Statistical distributions of the measured material properties are summarized in the boxplots provided in Figures A9-A10. Porosity values of the 24 cubic specimens ranged from 0.02% to 46.92%, with a median of 1.33% and an mean value of 7.36 ± 13.89%. Four samples (N6, N8, N18, N20) exhibited markedly higher porosity (>25%), thereby substantially influencing the SD for the porosity analysis. The densest specimens (N3, N7, N13, N19) exceeded 99.95% relative density (8.897-8.898 g/cm³), whereas the lowest density was 53.08% (4.724 g/cm³).

ANOVA confirmed a robust model fit ($R^2$ = 0.951, $Q^2$ = 0.878), and the analysis identified HS as the most influential parameter affecting porosity and density. Overall, the majority of samples (15 out of 24) achieved a high density greater than 98%. A total of 11 test samples fulfilled the literature target of greater than 99% density. The corresponding boxplot is provided in Figure 1. The residual normal probability plot and the regression coefficient diagram for porosity are provided in 2 and Figure 3.

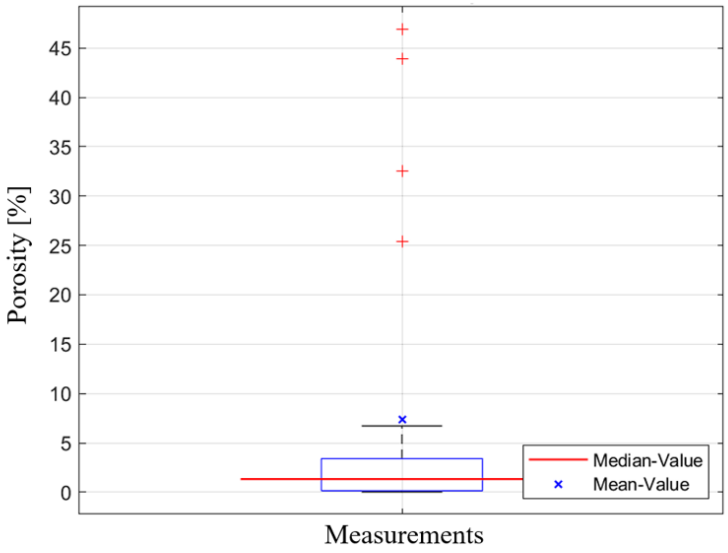


Figure 1: Boxplots of porosity values. Red lines indicate median values, and blue crosses denote mean values; whiskers represent data range and outliers.

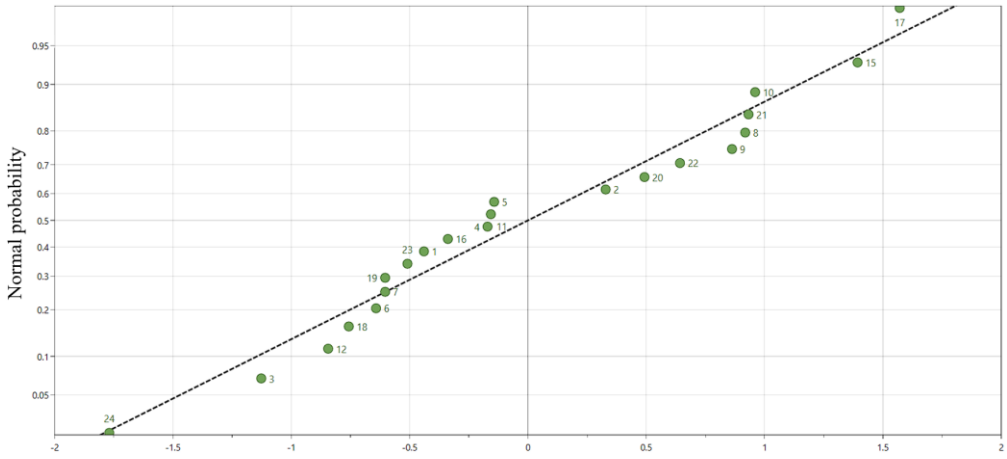


Figure 2: Residuals normal probability for the porosity model. Linear fit: $y = 1.119x + 3.25 \times 10^{-7}$. Model performance: N = 22, DF = 16, $R^2$ = 0.951, $Q^2$ = 0.878.

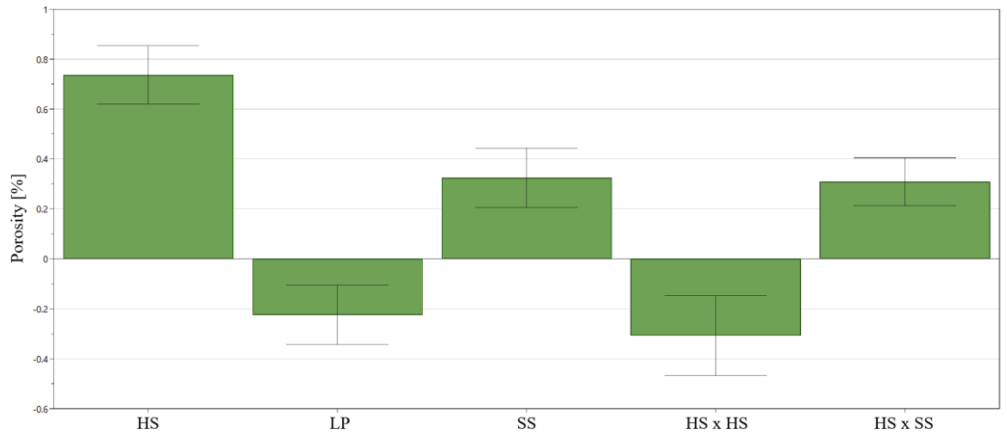


Figure 3: Regression coefficients (scaled and centered) for porosity with 95% confidence intervals. Model performance: N = 22, DF = 16, $R^2$ = 0.951, $Q^2$ = 0.878.

Hardness values ranged from 76.9 HV to 406.4 HV, with a mean of 336.5 ± 104.6 HV and a median of 381.7 HV. Most samples exceeded the ASTM F75 minimum requirement of 250 HV, while four specimens (N6, N8, N18, N20) showed markedly lower values due to high porosity. ANOVA confirmed a strong model fit ($R^2$ = 0.924, $Q^2$ = 0.805), and coefficient analysis identified HS and its interactions with SS and LP as the most influential factors on hardness. The majority of samples demonstrated sufficiently high hardness even without post-processing. UTS ranged from 207.7 MPa to 1140.2 MPa, with a mean of 906.7 ± 283.3 MPa. Four porous samples (N6, N8, N18, N20) fell below the ASTM F75 requirement of 655 MPa, while the remaining 83% exceeded this limit. The ANOVA model for UTS showed a predictive quality of $Q^2$ = 0.822 with $R^2$ = 0.931. HS and its interactions were identified as the most influential parameters. Yield strength ranged from 184.2 MPa to 747.0 MPa (mean 602.5 ± 164.7 MPa), with 75% of samples above the ASTM F75 minimum of 450 MPa. Elongation at break varied between 0.5% and 25% (median 10.9%), with several porous specimens fracturing prematurely and thus limiting ductility assessment. Stress–strain curves showed homogeneous plastic deformation until fracture. The combined influence of process parameters on porosity, hardness, UTS, and elongation is illustrated in the response contour maps visible in Figures 4-7.

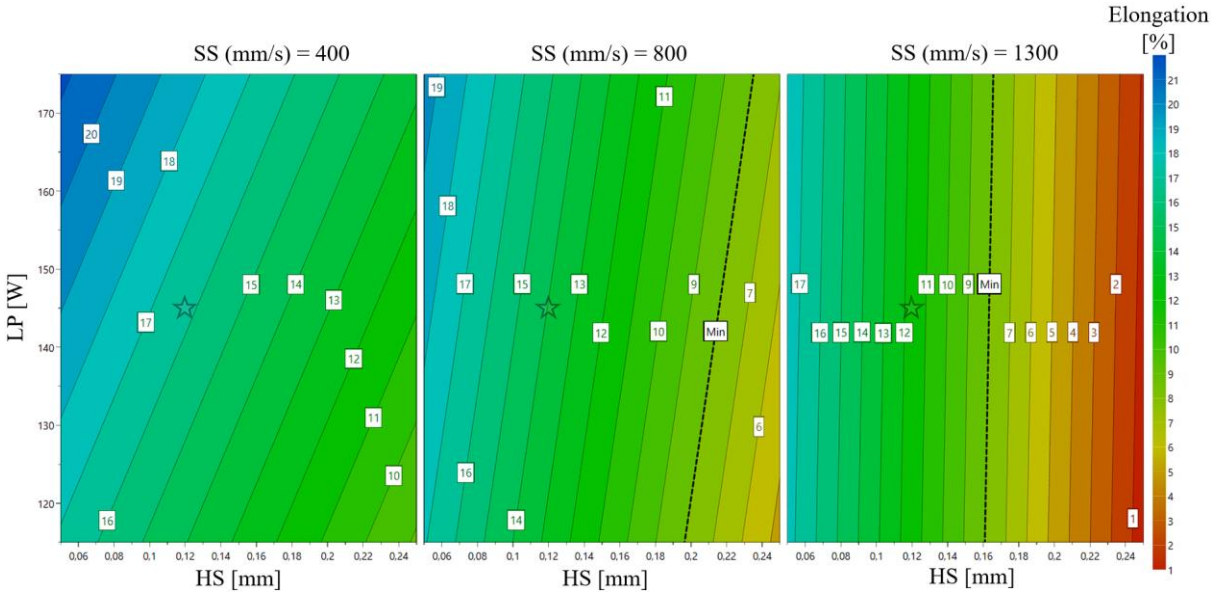


Figure 4: Response contour maps for elongation [%] as a function of HS and LP at fixed scan speeds (SS = 400, 800, 1300 mm/s; left to right). Dashed isolines indicate constraints (min/target where applicable); the star marks the robust set point identified in the design space analysis.

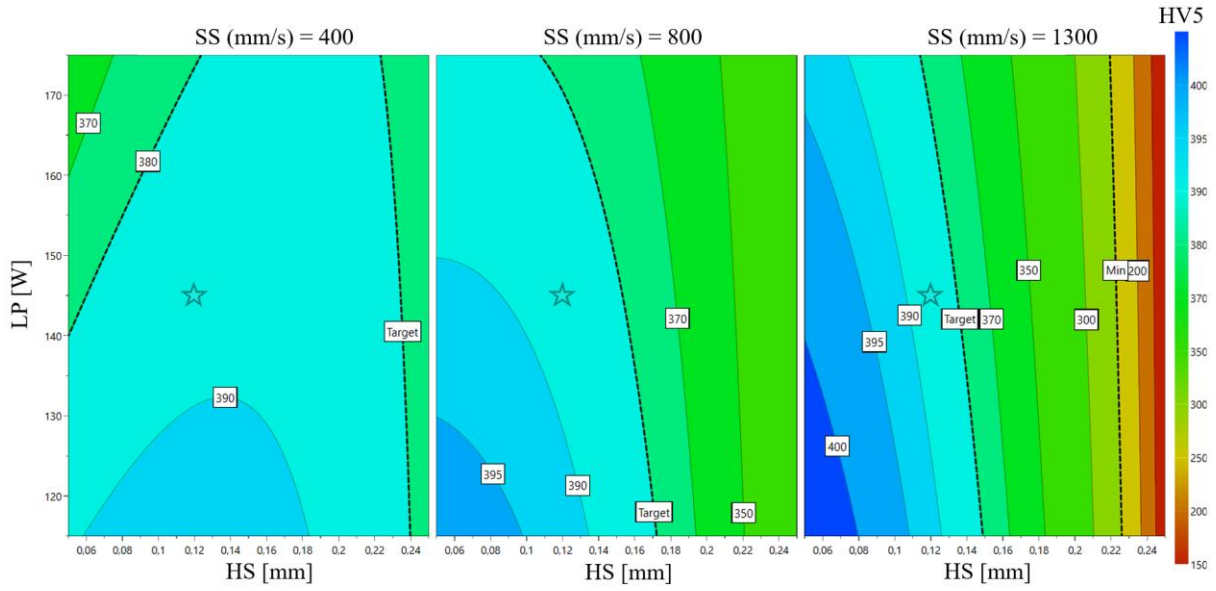


Figure 5: Response contour maps for hardness $HV_5$ as a function of HS and LP at fixed scan speeds (SS = 400, 800, 1300 mm/s; left to right). Dashed isolines denote specification thresholds (e.g., target/min); the star marks the robust set point.

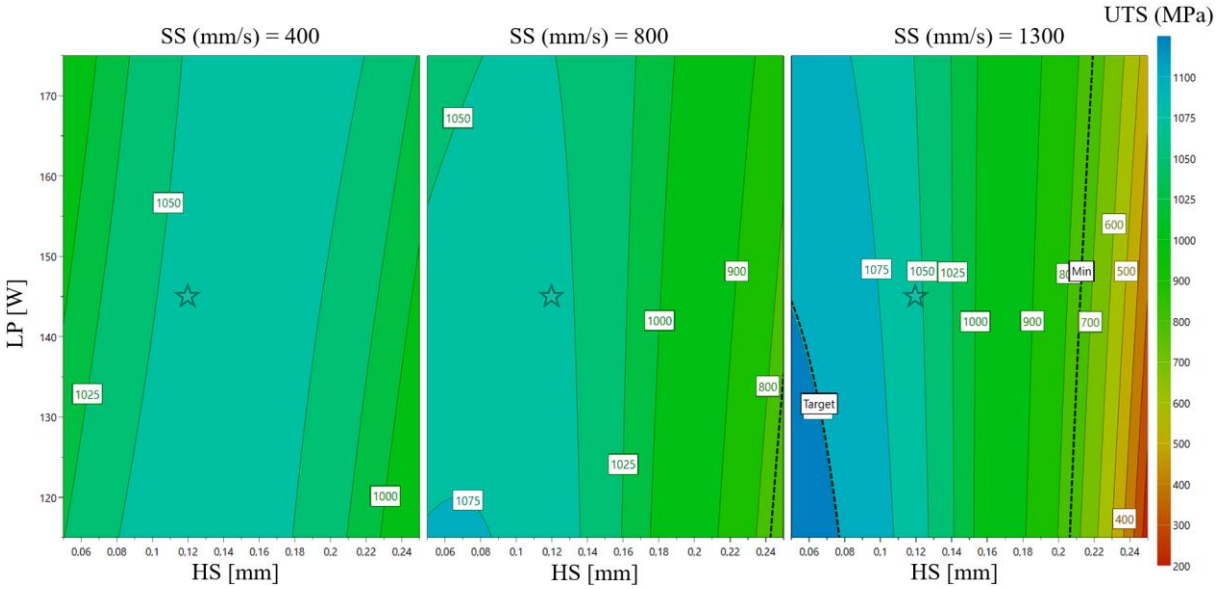


Figure 6: Response contour maps for porosity [%] as a function of HS and SS at fixed laser powers (LP = 115, 145, 175 W; left to right). Dashed isolines mark target/limit contours; the star denotes the robust set point.

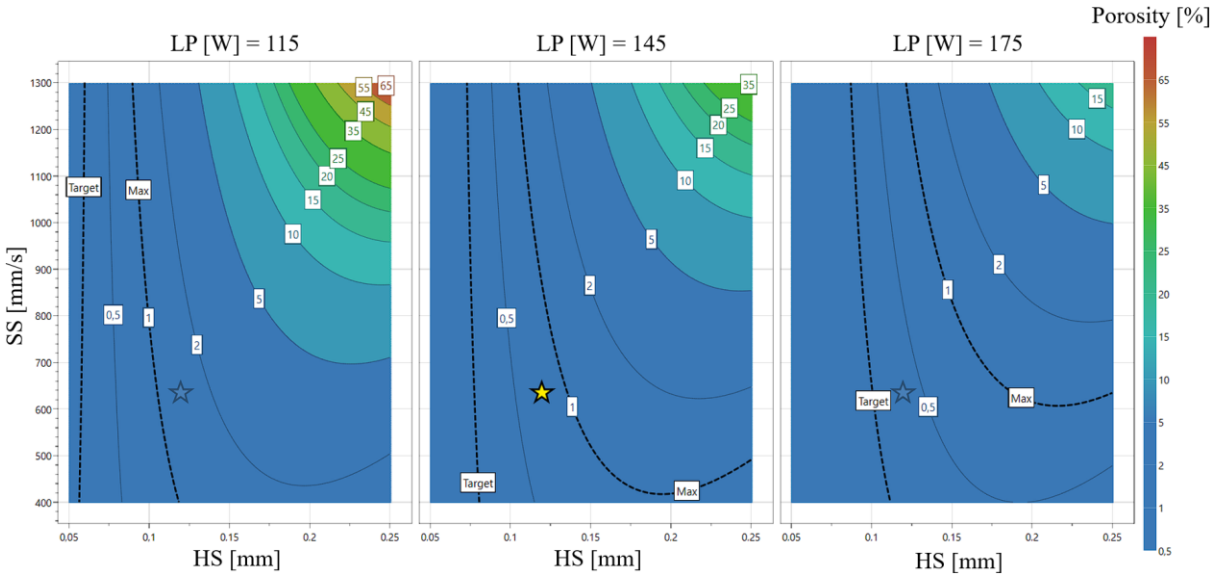


Figure 7: Response contour maps for porosity [%] as a function of HS and SS at fixed laser powers (LP = 115, 145, 175 W; left to right). Dashed isolines mark target/limit contours; the star denotes the robust set point.

Total pore counts varied strongly, with values spanning several orders of magnitude. Pore density ranged from 0.26 to 31.2 pores/mm², and mean pore radius values indicated a predominance of micro- and mesopores, while macropores were rare. The standard deviation of pore radius showed narrow distributions for dense samples, in contrast to broader and more irregular profiles in porous specimens. Outlier samples (N6, N8, N18, N20) exhibited visually larger, non-uniformly distributed pores; therefore, they could not

be quantified in greater detail (e.g., total pore count) except for density values. In contrast, most samples displayed homogeneous microstructural features with consistent pore sizes and distributions. To provide a quantitative overview of the pore distribution, Table A6 summarizes the 2D pore statistics for representative samples. Response surface analysis (Figure 8) identified an optimum for the process parameters at LP = 165.5 W, SS = 714 mm/s, HS = 63 µm. This setting predicted values for densities above 99.75%, hardness above 365 HV, UTS above 1000 MPa, and elongation of 16%.

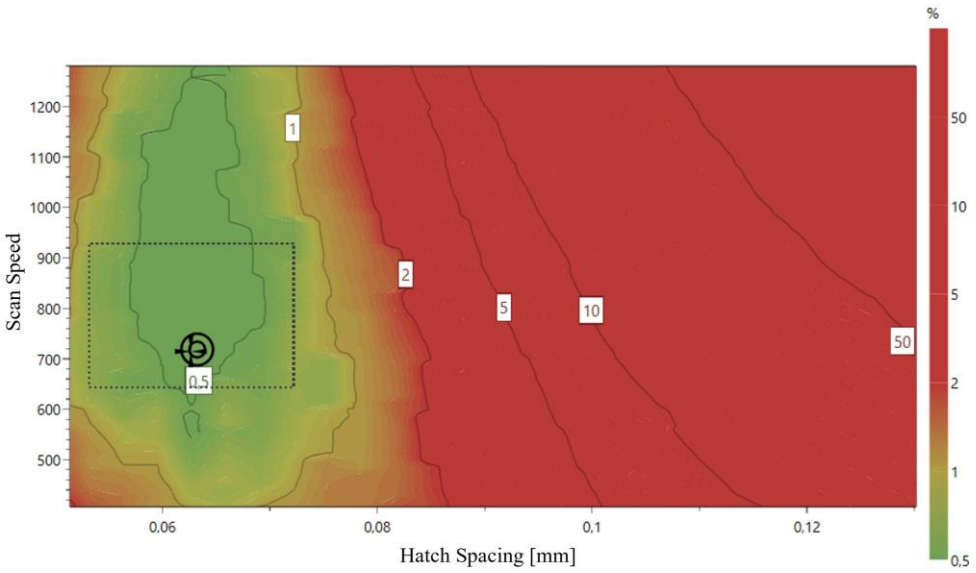


Figure 8: Design space for the probability of failure referring to the surpassing of material property thresholds; HSxSS at LP = 165.5 W; Marker shows most robust set point; Resolution = 64; Iterations = 10000; Acceptance level = 1% probability of failure; Factor contribution of HS ~55%, SS ~20%, LP ~25%; Dotted frame represents the largest possible regular hypercube that can fit into the irregular design space volume

Four additional samples were manufactured for model validation by mean absolute error (MAE). Two samples are manufactured with the optimized parameter combination to validate the predicted outcome. Additionally, two samples with parameters different from those previously tested were fabricated to validate the predictive power of the MODDE model. The predicted properties are listed in Table 3. Resulting measurements of the additional samples are listed in Table 4.

Table 3: Predicted values of the experimental validation with different process parameters.

| Sample | HS [mm] | LP [W] | SS [mm/s] | Porosity [%] | Hardness [HV5] | UTS [%] | Elongation [%] |
|---|---|---|---|---|---|---|---|
| V1 | 0.063 | 165.5 | 714 | 0.102 | 381.5 | 1035.8 | 18.8 |
| V2 | 0.063 | 165.5 | 714 | 0.102 | 381.5 | 1035.8 | 18.8 |
| V3 | 0.100 | 140.0 | 900 | 0.649 | 390.3 | 1065.0 | 14.8 |
| V4 | 0.125 | 170.0 | 500 | 0.396 | 381.1 | 1054.1 | 17.2 |

Table 4: Measured values for the experimental validation.

| Sample | HS [mm] | LP [W] | SS [mm/s] | Porosity [%] | Hardness [HV5] | UTS [%] | Elongation [%] |
|---|---|---|---|---|---|---|---|

| | | | | | | | |
|---|---|---|---|---|---|---|---|
| V1 | 0.063 | 165.5 | 714 | 0.15 | 386.0 | 1094.6 | 21.0 |
| V2 | 0.063 | 165.5 | 714 | 0.13 | 373.4 | 1060.5 | 18.8 |
| V3 | 0.100 | 140.0 | 900 | 0.52 | 403.4 | 1142.2 | 17.4 |
| V4 | 0.125 | 170.0 | 500 | 0.41 | 379.2 | 1071.6 | 18.4 |

The MAE shows a valid predictive power for the different models, resulting in $MAE_{dens/por}$ = 0.055%, $MAE_{hard}$ = 6.9 HV, $MAE_{UTS}$ = 44.5 MPa, and $MAE_{elong}$ = 1.5%. These values underline the predictive power and validation of the MODDE model.

## Discussion

The results confirm HS as the most critical parameter for densification in the tested parameter ranges. Larger distances between scan tracks promoted lack-of-fusion defects, while smaller values facilitated uniform overlap and reduced porosity. SS and LP showed secondary but consistent effects: excessive speed limited energy input and increased porosity, whereas higher power stabilized melt pools and improved bonding. These findings emphasize that process quality is potentially governed by the interaction of parameters rather than by isolated settings. In comparison with existing studies, the trends for SS and LP are largely consistent. Earlier investigations reported that higher SS tend to decrease relative density, while increased LP improves consolidation until excessive values induce keyholing [6, 11, 15]. Within the studied range, no keyhole porosity was observed, supporting the conclusion that increased power can enhance density to a certain threshold [16]. In previous work HS was often used at a fixed value [7, 17], and therefore its influence might be underestimated. The explicit variation conducted here demonstrates its dominant role, complementing and extending earlier conclusions about the importance of HS influenced meltpool overlap [9]. The mechanical response mirrors these porosity trends. Dense samples showed high hardness and tensile performance, while porous specimens consistently failed to meet ASTM requirements. Again, HS emerged as the strongest factor: insufficient overlap reduced hardness, UTS, and elongation, whereas smaller HS values supported dense structures with superior properties. SS and LP modulated these effects, with moderate values promoting stability by potentially forming fine grain structures in line with earlier reports [5, 6]. This assumption is also supported by the results of pore analysis, which emphasize that pore density, size, and distribution might collectively govern the microstructural quality and thereby influence the measured mechanical properties. The strong interdependence between porosity and mechanical properties thus underlines that minimizing defects is the potential key strategy to achieving reliable performance. The optimization analysis further confirmed the need for a balanced parameter set. HS again proved decisive, while moderate SS and higher LP might have stabilized melt pools and reduced lack-of-fusion defects. The resulting window offers a robust compromise between density, hardness, UTS, and elongation, ensuring compliance with ASTM F75 requirements. These results align with broader literature that stresses multi-parameter optimization [18, 19], but they go beyond simplified descriptors such as volumetric energy density (VED) [6, 7], which might obscure the critical role of HS. The finding that optimized PBF-LB/M conditions deliver superior properties compared to cast alloys is consistent with earlier reports [20, 21]. Overall, robust PBF-LB/M processing of Co28Cr6Mo requires systematic strategies that account for the combined effects of HS, SS, and LP to deliver reproducible high-performance parts for medical applications. While the study defines a robust process window for Co28Cr6Mo, some methodological constraints

should be considered. The two-level factorial design limited the resolution of higher-order interactions, and parameters such as LT, LSS, and scan strategy remained constant. Cubes were produced from fresh powder, whereas tensile samples were built using a 50/50 blend of fresh and recycled powder, which may have influenced porosity and mechanical response. Porosity evaluation was restricted to 2D metallographic sections using threshold segmentation; volumetric techniques such as micro computed tomography (µCT) could provide additional insight and link defect morphology to mechanical properties. All samples featured simple geometries without overhangs or support-dependent regions, which may not fully replicate the thermal histories or stress states of complex medical implants. Validation on benchmark or implant-like geometries will therefore be essential to confirm process transferability under application-relevant conditions.

## Conclusion

This study systematically investigated the processability of Co28Cr6Mo alloy on the TruPrint 1000 system using a two-level full factorial design. The parametric influence of HS, LP, and SS on density, porosity, hardness, elongation, and UTS was quantified. HS emerged as the most critical factor, exerting the strongest effect on densification, porosity suppression, and mechanical performance. LP and SS exhibited highly influential behavior but secondary contributions, with their interaction potentially further stabilizing melt pool dynamics and part quality. The optimized parameter set (LP of 165.5 W, SS of 714 mm/s, HS of 63 µm, with constant LSS of 55 µm and LT of 20 µm) exhibited a VED of 187 J/mm³ and produced parts exceeding the ASTM F75 requirements by a substantial margin. Densities above 99.75% and high strength levels confirm the suitability of this parameter window for high-quality, load-bearing biomedical applications. Beyond identifying optimal parameters, the predictive modeling framework proved effective for describing process-property relationships and minimizing the probability of failure. While the present findings are restricted to simplified geometries and a limited parameter space, they provide a robust foundation for extending PBF-LB/M process optimization toward clinically relevant Co28Cr6Mo implant geometries, including scapula applications.

## Declarations

- Please note: The number of samples per parameter set was not chosen arbitrarily but is a direct outcome of the statistically planned Design of Experiments. The design achieved a statistical power of 96%, indicating that the chosen sample size is sufficient for statistically reliable conclusions.
- Funding: Bayerische Staatsministerium für Wirtschaft, Landesentwicklung und Energie, Bayerisches Verbundforschungsprogramm des Freistaates Bayern – Förderlinie Digitalisierung (BayVFP), Projektkurzname PSchlAFSim, Förderkennzeichen DIK0396
- Conflict of interest/Competing interests: Not applicable.
- Ethics approval and consent to participate: Not applicable.
- Consent for publication: Not applicable.
- Data availability: The datasets generated and analyzed during the current study, including laboratory notes and prediction spreadsheets, are available from the corresponding author upon reasonable request.
- Materials availability: The specific Co28Cr6Mo powder (MetcoAdd F-75A) is commercially available.

- Code availability: The MATLAB scripts developed for porosity and density analysis are available from the corresponding author upon reasonable request.

## Extended Data

Table A1: Summary of the experimental design configuration used.

| Details | |
|---|---|
| Design Type | Full factorial (2-level) |
| Number of Runs | 24 (including 4 center points and 1 replicate) |
| Factors | 3 controlled, 2 constant |
| Model Structure | First-order with two-factor interactions |
| Statistical Power | 96% |

Table A2: Definition of quantitative process parameters used as factors in the screening DoE.

| Parameter | Unit | Role | Range/Setting |
|---|---|---|---|
| Hatch Spacing | mm | Controlled | 0.05-0.25 |
| Laser Power | W | Controlled | 115-175 |
| Scan Speed | mm/s | Controlled | 400-1300 |
| Layer Thickness | mm | Constant | 0.02 |
| Laser Spot Size | mm | Constant | 0.055 |

Table A3: Definition of response variables and corresponding optimization objectives for the screening DoE.

| Response | Unit | Objective | Min | Target | Max |
|---|---|---|---|---|---|
| Density | % | Target | 99 | 99.75 | 100 |
| Porosity | % | Target | - | 0.25 | 1 |
| Microhardness | HV | Maximize | 250 | 380 | 410 |
| Ultimate tensile strength | MPa | Maximize | 655 | 1100 | - |
| Elongation | % | Maximize | 8 | - | 25 |

Table A4: Process parameters for sample manufacturing (RO = Running Order).

| Sample | RO | HS | LP | SS | LT | LSS |
|---|---|---|---|---|---|---|
| - | - | [mm] | [W] | [mm/s] | [mm] | [mm] |
| N1 | 17 | 0.05 | 115 | 400 | 0.02 | 0.055 |
| N2 | 5 | 0.25 | 115 | 400 | 0.02 | 0.055 |
| N3 | 21 | 0.05 | 175 | 400 | 0.02 | 0.055 |
| N4 | 7 | 0.25 | 175 | 400 | 0.02 | 0.055 |
| N5 | 1 | 0.05 | 115 | 1300 | 0.02 | 0.055 |
| N6 | 9 | 0.25 | 115 | 1300 | 0.02 | 0.055 |

| | | | | | | |
|---|---|---|---|---|---|---|
| N7 | 22 | 0.05 | 175 | 1300 | 0.02 | 0.055 |
| N8 | 14 | 0.25 | 175 | 1300 | 0.02 | 0.055 |
| N9 | 15 | 0.15 | 145 | 850 | 0.02 | 0.055 |
| N10 | 20 | 0.15 | 145 | 850 | 0.02 | 0.055 |
| N11 | 8 | 0.15 | 145 | 850 | 0.02 | 0.055 |
| N12 | 6 | 0.15 | 145 | 850 | 0.02 | 0.055 |
| N13 | 18 | 0.05 | 115 | 400 | 0.02 | 0.055 |
| N14 | 24 | 0.25 | 115 | 400 | 0.02 | 0.055 |
| N15 | 11 | 0.05 | 175 | 400 | 0.02 | 0.055 |
| N16 | 2 | 0.25 | 175 | 400 | 0.02 | 0.055 |
| N17 | 23 | 0.05 | 115 | 1300 | 0.02 | 0.055 |
| N18 | 16 | 0.25 | 115 | 1300 | 0.02 | 0.055 |
| N19 | 19 | 0.05 | 175 | 1300 | 0.02 | 0.055 |
| N20 | 13 | 0.25 | 175 | 1300 | 0.02 | 0.055 |
| N21 | 10 | 0.15 | 145 | 850 | 0.02 | 0.055 |
| N22 | 4 | 0.15 | 145 | 850 | 0.02 | 0.055 |
| N23 | 12 | 0.15 | 145 | 850 | 0.02 | 0.055 |
| N24 | 3 | 0.15 | 145 | 850 | 0.02 | 0.055 |

Table A5: Summary of filters applied during MATLAB-based image analysis.

| Filter | Purpose |
|---|---|
| Gaussian | Smooths the image and reduces high-frequency noise |
| Median | Replaces each pixel with the median of neighboring values, preserving edges |
| Anisotropic | Enhances pore structures while suppressing background noise |
| Anisotropic Diffusion | Reduces speckle noise and improves contrast |

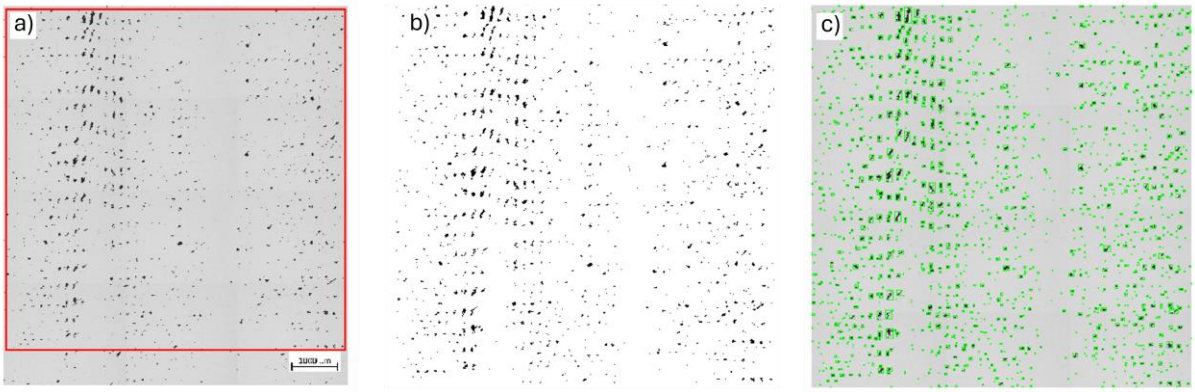


Figure A1: Before and after image processing of sample N10. a) Original image with marked area for analysis (scale: 1000 µm); b) Binary mask of the image; c) Segmentation overlay of the detected pores.


Figure A2: Overview of the tensile specimens after destructive tensile testing, showcasing the breakpoint of each sample; scale: 10 mm.

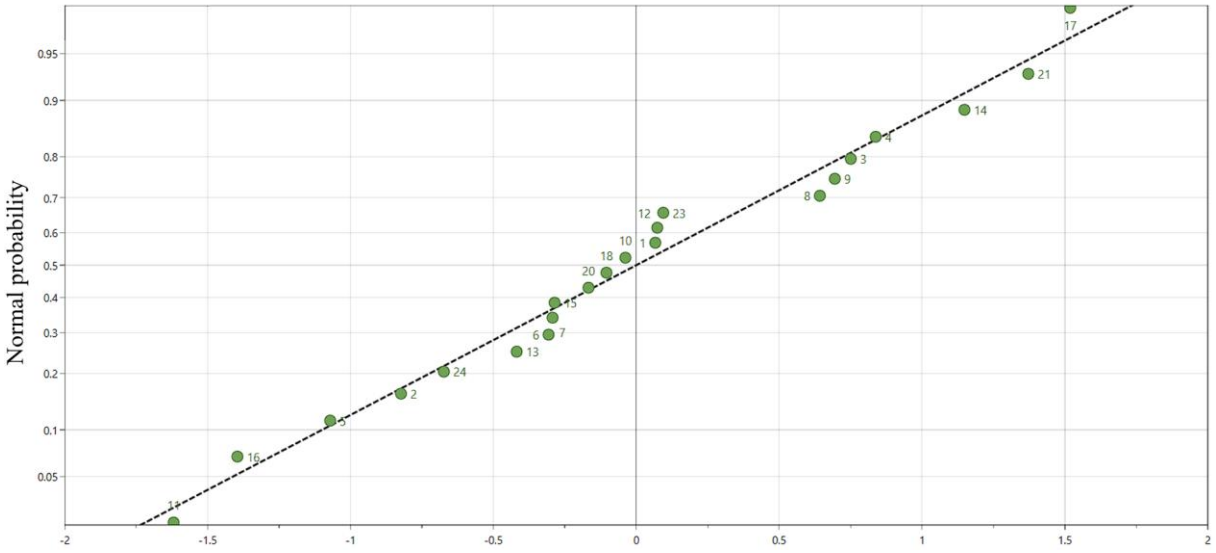


Figure A3: Residuals normal probability for the hardness $HV_5$ model. Linear fit: $y = 1.165x + 8.93*10^{-7}$. Model performance: N = 22, DF = 15, $R^2 = 0.924$, $Q^2 = 0.805$.

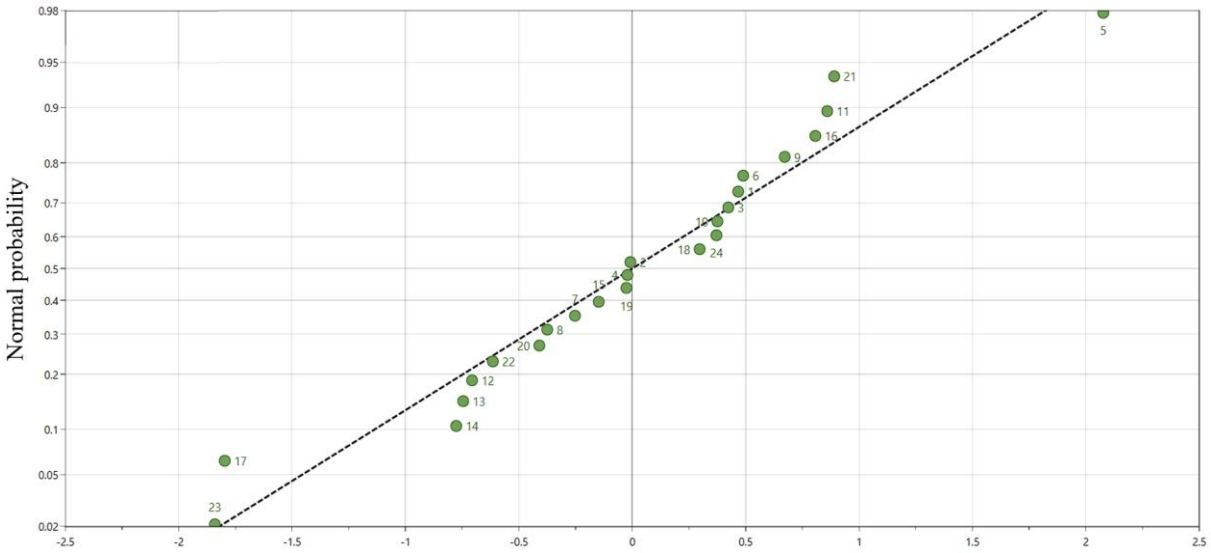


Figure A4: Residuals normal probability for the UTS model. Linear fit: $y = 1.129x + 3.85*10^{-7}$. Model performance: N = 24, DF = 17, $R^2 = 0.931$, $Q^2 = 0.822$.

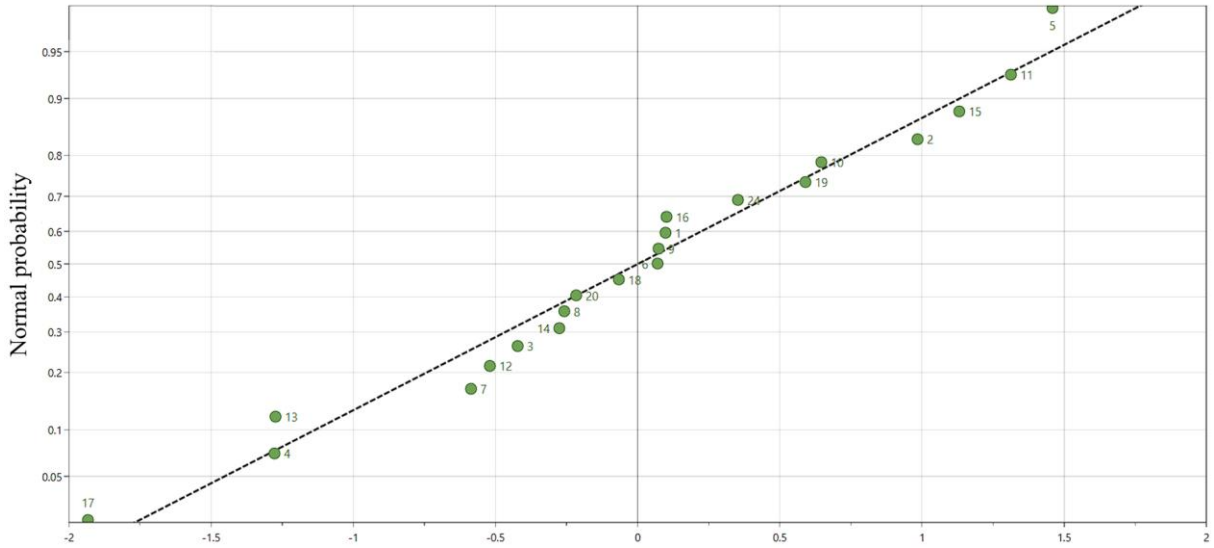


Figure A5: Residuals normal probability for the elongation model. Linear fit: $y = 1.132x + 1.71*10^{-5}$. Model performance: N = 21, DF = 15, $R^2 = 0.961$, $Q^2 = 0.869$.

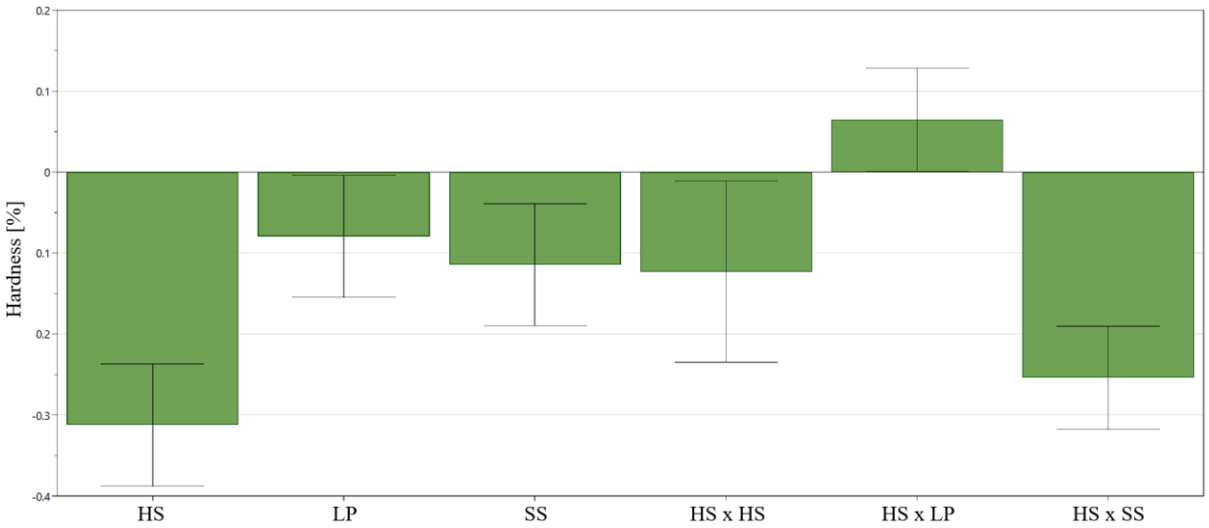


Figure A6: Regression coefficients for Hardness $HV_5$ with 95% confidence intervals. Model performance: N = 22, DF = 15, $R^2$ = 0.924, $Q^2$ = 0.805.

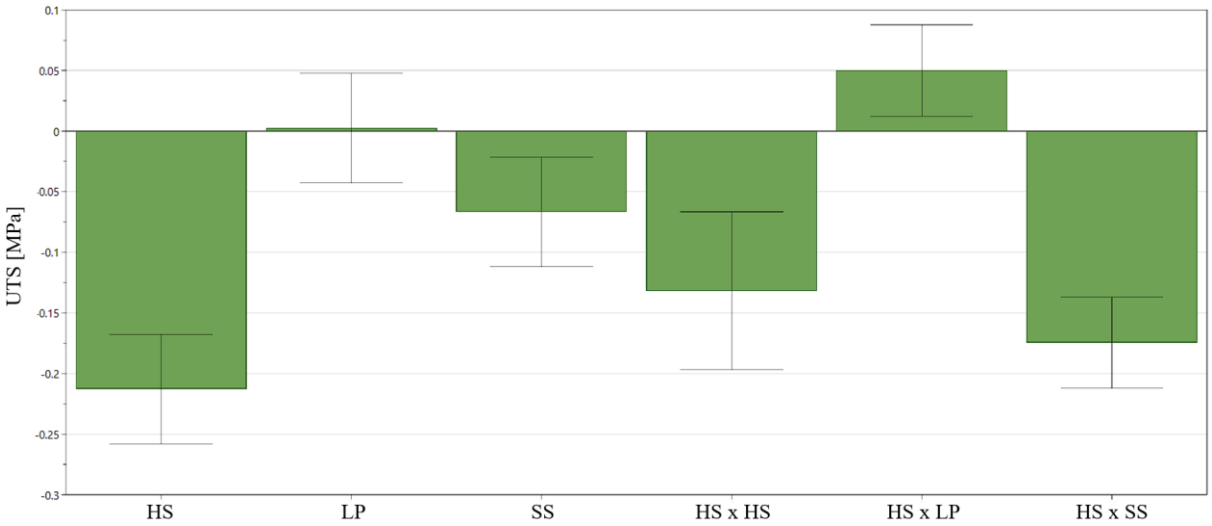


Figure A7: Regression coefficients for UTS with 95% confidence intervals. Model performance: N = 24, DF = 17, $R^2$ = 0.931, $Q^2$ = 0.822.

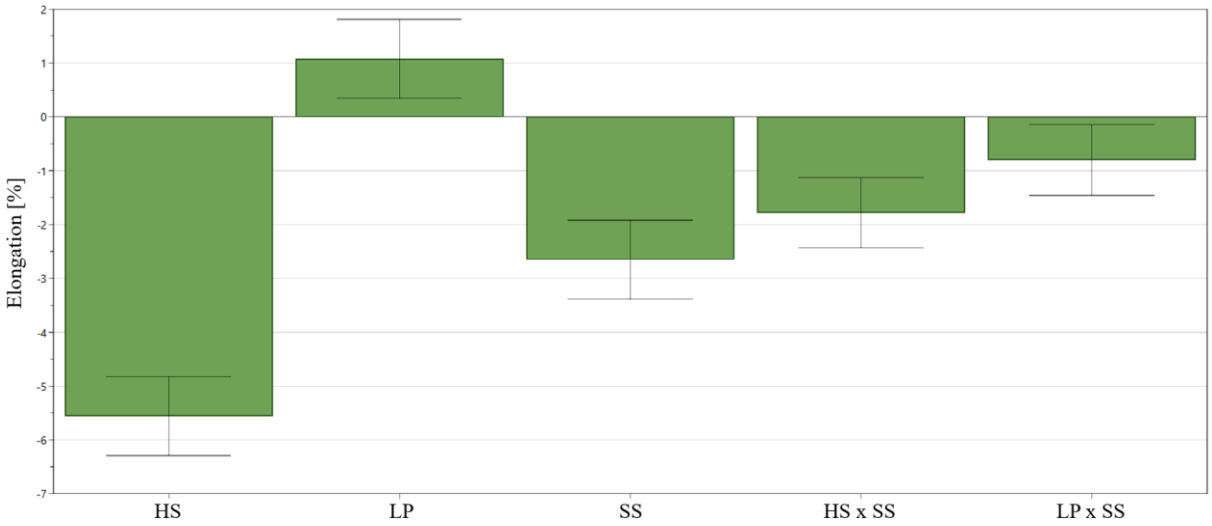


Figure A8: Regression coefficients for elongation with 95% confidence intervals. Model performance: N = 21, DF = 15, $R^2$ = 0.961, $Q^2$ = 0.869.

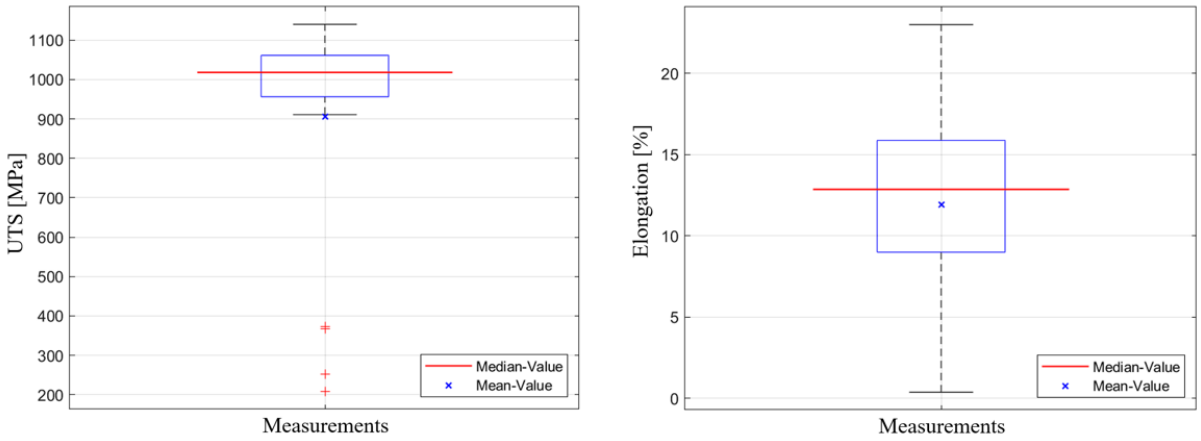


Figure A9: Boxplots of UTS and elongation across all measured specimens. Red lines indicate median values, and blue crosses denote mean values; whiskers represent data range and outliers.

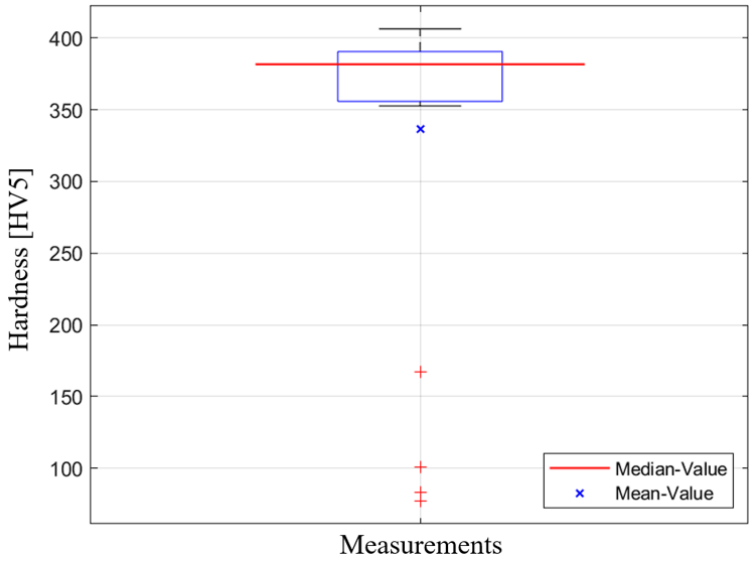


Figure A10: Boxplots of $HV_5$ across all measured specimens. Red lines indicate median values, and blue crosses denote mean values; whiskers represent data range and outliers.

Table A6: Summary of 2D pore statistics for selected PBF-LB/M-fabricated Co28Cr6Mo samples (excluding highly porous specimens N6, N8, N18, and N20)

| Sample | Micro-pores | Meso-pores | Macro-pores | Total pores | Pore density |
|---|---|---|---|---|---|
| - | [n] | [n] | [n] | [n] | [n/mm²] |
| N1 | 123 | 95 | 0 | 218 | 3.92 |
| N2 | 263 | 705 | 0 | 968 | 18.40 |
| N3 | 2 | 15 | 0 | 17 | 0.33 |
| N4 | 74 | 148 | 0 | 222 | 4.01 |
| N5 | 227 | 47 | 0 | 274 | 4.89 |
| N7 | 3 | 15 | 0 | 18 | 0.33 |
| N9 | 425 | 1012 | 0 | 1437 | 28.07 |
| N10 | 490 | 1147 | 0 | 1637 | 28.77 |
| N11 | 531 | 773 | 0 | 1304 | 23.44 |
| N12 | 255 | 556 | 0 | 811 | 14.45 |
| N13 | 3 | 11 | 0 | 14 | 0.26 |
| N14 | 427 | 819 | 7 | 1253 | 31.24 |
| N15 | 142 | 59 | 0 | 201 | 3.57 |
| N16 | 110 | 167 | 0 | 277 | 4.99 |
| N17 | 176 | 200 | 0 | 376 | 7.06 |
| N19 | 39 | 13 | 0 | 52 | 0.94 |
| N21 | 340 | 1163 | 0 | 1503 | 26.96 |
| N22 | 171 | 957 | 0 | 1128 | 20.50 |
| N23 | 714 | 670 | 0 | 1384 | 25.60 |
| N24 | 246 | 402 | 0 | 648 | 11.58 |

## Literatur


[1] Kennedy, S.M., A, V., K, A.: Exploring the frontiers of metal additive manufacturing in orthopaedic implant development. MethodsX 13, 103056 (2024) https://doi.org/10.1016/j.mex.2024.103056

[2] Mobarak, M.H., Islam, M.A., Hossain, N., Al Mahmud, M.Z., Rayhan, M.T., Nishi, N.J., Chowdhury, M.A.: Recent advances of additive manufacturing in implant fabrication – a review. Applied Surface Science Advances 18, 100462 (2023) https://doi.org/10.1016/j.apsadv.2023.100462

[3] C. Yao, J. Lu, T.J. Webster: 2 - titanium and cobalt–chromium alloys for hips and knees. In: Michael Lysaght, Thomas J. Webster (eds.) Biomaterials for Artificial Organs. Woodhead Publishing Series in Biomaterials, pp. 34–55. Woodhead Publishing, Abington Hall, Granta Park Great Abington, Cambridge, United Kingdom (2011). https://doi.org/10.1533/9780857090843.1.34

[4] Milosev, I.: Cocrmo alloy for biomedical applications. In: Djokic, S.S. (ed.) Biomedical Applications. Modern Aspects of Electrochemistry, vol. 55, pp. 1–72. Springer US, Boston, MA (2012). https://doi.org/10.1007/978-1-4614-3125-1_1

[5] Monroy, K.P., Delgado, J., Sereno, L., Ciurana, J., Hendrichs, N.J.: Effects of the selective laser melting manufacturing process on the properties of cocrmo single tracks. Metals and Materials International 20(5), 873–884 (2014) https://doi.org/10.1007/s12540-014-5011-0

[6] Li, H., Song, B., Wang, Y., Zhang, J., Zhao, W., Fang, X.: Laser powder bed fusion process optimization of cocrmo alloy assisted by machine-learning. Journal of Materials Research and Technology 33, 3901–3910 (2024) https://doi.org/10.1016/j.jmrt.2024.10.075

[7] Liu, W., Xie, Q., Cao, Y., Wang, J., Bai, P.: Optimization of processing parameters for lpbf-manufactured cocr alloys based on laser volume energy density. Journal of Materials Research and Technology 27, 4053–4063 (2023) https://doi.org/10.1016/j.jmrt.2023.10.268

[8] Ciurana, J., Hernandez, L., Delgado, J.: Energy density analysis on single tracks formed by selective laser melting with cocrmo powder material. The International Journal of Advanced Manufacturing Technology 68(5-8), 1103–1110 (2013) https://doi.org/10.1007/s00170-013-4902-4

[9] Weaver, J.S., Heigel, J.C., Lane, B.M.: Laser spot size and scaling laws for laser beam additive manufacturing. Journal of Materials Processing Technology 73 (2022) https://doi.org/10.1016/j.jmapro.2021.10.053.

[10] Pupo, Y., Delgado, J., Seren´o, L., Ciurana, J.: Scanning space analysis in selective laser melting for cocrmo powder. Procedia Engineering 63, 370–378 (2013) https://doi.org/10.1016/j.proeng.2013.08.228

[11] Wang, J.-H., Ren, J., Liu, W., Wu, X.-Y., Gao, M.-X., Bai, P.-K.: Effect of selective laser melting process parameters on microstructure and properties of co-cr alloy. Materials (Basel, Switzerland) 11(9) (2018) https://doi.org/10.3390/ma11091546

[12] Oerlikon Metco: Material Product Data Sheet: Cobalt - Chromium – Molybdenum Alloy Powders for Additive Manufacturing: Material Product Data Sheet. Available online at Oerlikon; accessed on 18.10.2025 (2022)

[13] Arcam AB: ASTM F75 Cobalt Chrome Alloy. Available online at https://static.treatstock.com/static/fxd/wikiMaterials/Cobalt-Chrome/files/arcam-astm-f75-cobalt-chrome.pdf; accessed on 18.10.2025 (2007)

[14] Sartorius Stedim Data Analytics AB: MODDE® 12 User Guide. Available online at https://www.sartorius.com/download/544636/modde-12-user-guide-en-b-00090-sartorius-data.pdf; accessed on 18.10.2025 (2017)

[15] Song, C., Yang, Y., Wang, Y., Di Wang, Yu, J.: Research on rapid manufacturing of cocrmo alloy femoral component based on selective laser melting. The International Journal of Advanced Manufacturing Technology 75(1-4), 445–453 (2014) https://doi.org/10.1007/s00170-014-6150-7

[16] Konieczny, B., Szczesio-Wlodarczyk, A., Sokolowski, J., Bociong, K.: Challenges of co-cr alloy additive manufacturing methods in dentistry-the current state of knowledge (systematic review). Materials (Basel, Switzerland) 13(16) (2020) https://doi.org/10.3390/ma13163524

[17] Ma, L.Y., Sun, F.Y., Li, Y., Yu, H.: Mechanical property, corrosion behavior and cytocompatibility of cocrmo for dental application: A comparative study of cast and laser powder bed fusion. Journal of the mechanical behavior of biomedical materials 160, 106788 (2024) https://doi.org/10.1016/j.jmbbm.2024.106788

[18] Chia, H.Y., Wu, J., Wang, X., Yan, W.: Process parameter optimization of metal additive manufacturing: a review and outlook. Journal of Materials Informatics 2(3), 16 (2022) https://doi.org/10.20517/jmi.2022.18

[19] Videršsčak, D., Schauperl, Z., Runje, B., ˇSoli´c, S., ´Cati´c, A., Godec, M., Paulin, I., Donik, ˇC.: Laser powder bed fusion parameters optimization for enhanced mechanical properties of eos co-cr dental alloy. Materials (Basel, Switzerland) 17(20) (2024) https://doi.org/10.3390/ma17204993

[20] Dolgov, N., Dikova, T., Dzhendov, D., Pavlova, D., Simov, M.: Mechanical properties of dental co-cr alloys fabricated via casting and selective laser melting. International Journal “Materials Science. Non-Equilibrium Phase Transformations”, 3–7 (2016)

[21] Nabizadeh Dizaj, M., Azarbarmas, M., Abdi, A.: The influence of heat treatment on the microstructure, hardness, and wear properties of cocrmo alloy produced by powder bed fusion of metals using a laser beam (pbf-lb/m) process. Progress in Additive Manufacturing (2024) https://doi.org/10.1007/s40964-024-00895-4

## Kontaktangaben

Kevin Lippmann
Hochschulstr. 1
83024 Rosenheim
Deutschland
E-Mail: kevin.lippmann@th-rosenheim.de
WEB: Laboratory of Additive Manufacturing